Pore-scale study of pore-ionomer interfacial reactive transport processes in proton exchange membrane fuel cell catalyst layer

Li Chen[a,*], Ruiyuan Zhang[a], Qinjun Kang[b], Wen-Quan Tao[a]

[a] Key Laboratory of Thermo-Fluid Science and Engineering of MOE, School of Energy and Power Engineering, Xi'an Jiaotong University, Xi'an, Shaanxi 710049, China
[b] Earth and Environmental Sciences Division, Los Alamos National Laboratory, Los Alamos, NM, USA

HIGHLIGHTS

- Pore-scale reactive transport processes in catalyst layer are numerically studied.
- High resolution porous structures of multiphase catalyst layer are reconstructed.
- Complex pore-ionomer interfacial reactive transport processes are considered.
- Optimum ionomer content generating best cell performance is evaluated.
- Optimum ionomer content maintaining performance under low Pt loading is assessed.

GRAPHICAL ABSTRACT
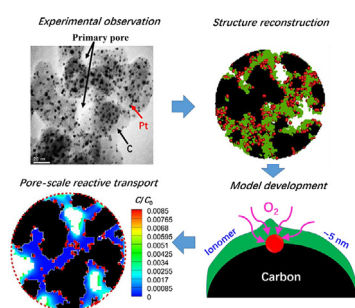
ARTICLE INFO

ABSTRACT

Understanding interactions between constituent distributions and reactive transport processes in catalyst layer (CL) of proton exchange membrane fuel cell is crucial for improving cell performance and reducing cell cost. In this study, high-resolution porous structures of cathode CL are reconstructed, where all the constituents in CLs are resolved. A pore-scale model based on the lattice Boltzmann method is developed for oxygen diffusion in pores and ionomer, as well as electrochemical reaction at the Pt surfaces. Particularly the model considers the pore-ionomer interfacial transport processes with distinct characteristics of sharp concentration drop, large diffusivity ratio and interfacial dissolution reaction. After validated by interfacial transport processes with analytical solutions, the pore-scale model is applied to reactive transport processes inside complex CL nanoscale structures. Pore-scale results reveal that pore-ionomer interfacial transport processes generate extremely high local transport resistance, significantly reducing the total reaction rate. As volume fraction of carbon increases, the value of the optimum ionomer content generating the best cell performance decreases, while the value of the optimum ionomer content resulting in the lowest performance loss under low Pt loading reduces. The two values generally are different. The pore-scale model helps to understand reactive transport processes and to optimize the CL structures.

1. Introduction

Proton exchange membrane fuel cells (PEMFCs) have drawn great attention due to its advantages such as high efficiency, high power density, low pollution and room operating temperature. Performance and durability of PEMFC systems for automotive use have progressed

---

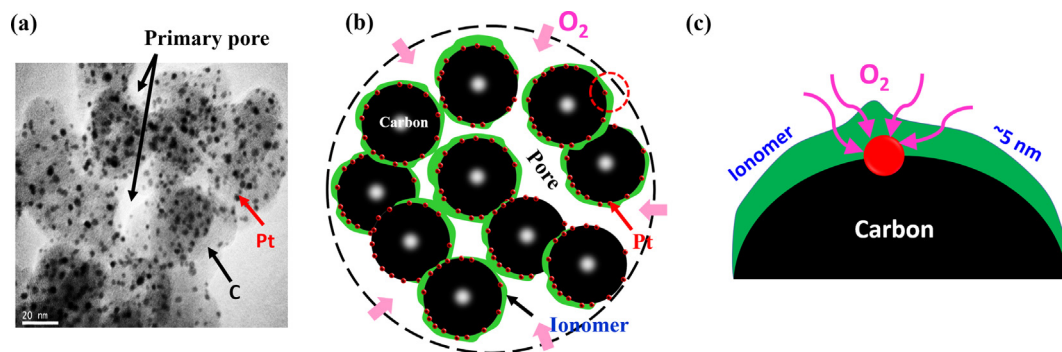**Fig. 1.** Structures, constituents and reactive transport processes in catalyst layers. (a) TEM image of CL (weight ratio of Pt to carbon Pt/C is 20%), (b) Schematic of multiple constituent distributions in carbon agglomerates and reactive transport processes of oxygen in pores between carbon particles, and (c) schematic of local transport processes of oxygen through the thin ionomer film to the Pt surface for electrochemical reaction.

dramatically during the past decade thanks to intensive research from both academia and industry. Yet problems hindering the successful commercialization of PEMFCs still remain. One is the cost of PEMFCs, which is still significantly higher than that of the internal combustion engine due to expensive Platinum (Pt) adopted in the porous electrodes of PEMFCs [1]. In both anode and cathode catalyst layers (CLs) of a PEMFC, electrochemical reactions take place, the kinetics of which is relatively slow, especially the oxygen reduction reaction (ORR) in the cathode side. To improve the chemical reaction rate, Pt is widely adopted as the catalyst. For successful commercialization of PEMFCs, it is required that the Pt loading be reduced below 0.1 mg cm^{-2} from current level of about 0.4 mg cm^{-2}, while the cell performance is still maintained.

Performance and cost of PEMFCs are significantly affected by CLs due to local transport limitations and poor ORR kinetics. The CLs currently widely adopted are porous media with heterogeneous structures and multiple constituents, consisting of carbon particles, Pt particles, electrolyte (Nafion) and void space, as shown in Fig. 1. Multiple transport processes simultaneously occur in CLs, including oxygen transport in void space and dissolution in Nafion, proton migration in Nafion, electron conduction in connected carbon spheres and Pt, as well as ORR at the triple-phase boundary (TPB) [2]. These processes are coupled and compete with each other. For example, increasing Nafion content improves proton conduction, but reduces void space and thus deteriorates the oxygen transport. Understanding such complex reactive transport processes in CLs has been a long and on-going activity for optimizing CL structures to enhance transport processes and to reduce Pt loading.

As part of the on-going activity, numerical simulation has played an important role due to its ability to provide detailed spatial distributions of important variables such as velocity field, temperature, species concentration, two-phase distribution, electrical potentials, and current density [2,3]. The typical thickness of CLs is about 10 μm, significantly smaller than the size of an entire PEMFC (cm). In cell-scale models the CL is usually treated as a thin interface, a homogeneous porous medium or agglomerates of carbon particles [2], corresponding to the thin-film interface model [4], the homogeneous model [5,6] and the agglomerate model [7]. In the above cell-scale models, the detailed porous structures and distributions of different constituents are not resolved. Instead, bulk-averaged geometrical properties are adopted to implicitly describe the CL structures, such as porosity, pore size distribution, specific surface area, tortuosity, etc. Such models are computationally efficient. However, they heavily depend on the accurate determination of effective transport properties such as permeability, effective thermal conductivity, effective diffusivity, etc. [8]. These effective transport properties are calculated by empirical relationships (for example, Bruggeman equation for diffusion, Kozeny-Carman equation for permeability). The accuracy of these relationships for porous electrodes of PEMFC needs further validation [9].

While the above continuum-scale models are actually phenomenological models at their best, pore-scale models directly resolve the nanoscale multiphase porous structures of CLs, and solve the first-principle equations for the reactive transport processes involved. Recently, the pore-scale models have gained increasing attention thanks to the development of computer technique, visualization techniques of complex structures, and advanced numerical methods. Wang et al. [10] conducted pore-scale simulations of oxygen transport, proton conduction and electrochemical reaction in a 2D idealized porous structure representing CLs. Later, the structure was extended to 3D random structures [11] and further to bilayer porous structures of CLs [12]. To model the typical length of CLs (10 μm), resolution of the above reconstructed structures was as low as 250 nm, thus the reconstructed structures only took into account two phases, with one as the pore phase and the other as mixtures of electrolyte and solid components.

Subsequently, structure reconstruction schemes with high resolution were developed [13–20]. Kim and Pitsch [13] proposed a simulated annealing technique to reconstruct CL structures with a resolution as high as 8 nm. Solid spheres with typical size of carbon particles in CLs were placed in the computational domain, and the simulated annealing technique was adopted to move these spheres to obtain desirable porosity and two-point correction function. A thin electrolyte film was then covered on the surface of the solid particles [13]. Siddique and Liu [15] proposed a reconstruction scheme based on the specific synthesis process of CL fabrication. The resolution of the reconstructed structure was as high as 2 nm, with all the four constituents (carbon, Pt, Nafion, and pore) in CLs accounted for. The above CL fabrication process based reconstruction scheme was later improved by Chen et al. to ameliorate the electrolyte connectivity [18]. Recently, a sphere chain controlled method was developed by Inoue et al. [19] to consider the aggregation strength of carbon particles, and large pores were also locally added to consider their effects on diffusion process.

With the complicated structures of CLs reconstructed, pore-scale reactive transport processes were studied using Computational Fluid Dynamics (CFD) methods such as finite volume method (FVM), finite element method (FEM), finite difference method (FDM). The mesoscopic lattice Boltzmann method (LBM) has also been widely adopted. Pore-scale oxygen diffusion, proton conduction and electron conduction processes have been studied [13–20]. Knudsen diffusion mechanism in the nanoscale pores has been incorporated into the transport processes [14]. Based on the pore-scale distributions of concentration and potential, effective transport properties were predicted and compared with existing empirical equations [14,17,18]. Electrochemical reaction at the TPB has been investigated and CL pore-scale structures were improved to enhance the CL performance [10,14]. Effects of pore-scale liquid water distributions on the transport processes also have been explored recently [21,22]. CL structures are also improved based on the pore-scale results to enhance the reactive transport processes [18,23].

The above numerical studies are helpful for enhancing the reactive

transport processes in CLs and thus for improving the Pt utilization. It is highly desirable that both the Pt loading and the transport resistance inside the CLs are reduced. Transport resistance inside the CLs includes two parts: bulk resistance resulting from bulk and Knudsen diffusion in pores between Pt/C particles, and local resistance related to diffusion in thin ionomer film, as schematically shown in Fig. 1(b) and (c), respectively. Recently, experiments have found that the transport resistance greatly increases in CLs under low Pt loading, leading to extra loss of the cell voltage [24]. For example, Greszler et al. [25] found that the local transport resistance greatly increases from 5 s m^{-1} under Pt loading 0.4 mg cm^{-2} to 20 s m^{-1} under Pt loading 0.1 mg cm^{-2}. Such high transport resistance leads to considerable loss of cell voltage under high current density.

Due to the nanoscale complex structures of CLs, currently direct measurement of the transport resistance is still infeasible, and ex-situ experiments based on measurement of the limiting current density have been widely adopted [26]. It was found that the extra transport resistance arises from the local oxygen transport processes in the nanoscale confined space of CLs, especially at the phase interface and inside the ionomer [25–30]. Without considering the local transport processes, the agglomerate model, which is state-of-the-art continuum-scale model of CLs, has to adopt extremely large size of agglomerate or extremely thick ionomer film (> 100 nm) covered on Pt/C, which is not consistent with experimental observations where the typical ionomer thickness is about 10 nm [30,31].

Currently, the mechanism of the extra transport resistance is still under investigation. Some researchers argued that diffusivity of oxygen in the thin ionomer film (~10 nm) is much lower than that in the bulk ionomer (> 1 μm) [32]. Kudo et al. [28] suggested that the dissolution reaction with limited reaction rate constant at the pore-ionomer interface is responsible for the extra transport resistance. By incorporating such non-equilibrium interfacial reaction into the agglomerate model, Hao et al. [31] found that the agglomerate model with the size of a carbon particle and with ionomer thickness typically observed in experiments can successfully predict the cell performance under low Pt loading. Chen et al. [33] proposed a pore-scale model around a carbon particle in which the interfacial dissolution reaction was taken into account. The pore-scale model was then adopted to study effects of dissolution reaction rate, Pt particle distribution and ionomer thickness on the local transport resistance. The local transport resistance numerically predicted with interfacial dissolution resistance considered was in good agreement with existing experimental results.

From the above review, it can be found that to further enhance reactive transport processes in CLs and to reduce the Pt loading, it is crucial to investigate the underlying mechanisms of the local reactive transport in CLs and to understand the interactions between distributions of multiple constituents (carbon, Pt, ionomer) and reactive transport processes. Therefore, in this study, a pore-scale model is developed for reactive transport processes within CLs in Section 2, with emphasis placed on the transport processes across interfaces of different constituents. Such local interfacial transport processes present the complicated characteristics of concentration jump, large diffusivity ratio and non-equilibrium dissolution reaction. To the best of our knowledge, this is the first time the above complex interfacial reactive transport processes are fully addressed and incorporated into a pore-scale reactive transport model of CLs. With the pore-scale model for interfacial transport processes developed and validated, it is then adopted to study pore-scale reactive transport processes in reconstructed CLs in Section 3. Effects of the interfacial transport on CL performance are explored in detail in Section 3. Finally, important conclusions are drawn in Section 4.

2. Porous structure reconstruction and pore-scale model development

Pore-scale model bridges the gap between continuum-scale models

and molecular-scale models. Continuum-scale models of PEMFCs provide transport information at the cell-scale (~cm) from the engineering viewpoint, while molecular-scale simulations provide underlying details at the molecular level (~nm). Thus, there is a significant gap between the length-scale studied and the transport phenomena provided between the continuum-scale and the molecular scale. Pore-scale model bridges the above disparity of length scale. In recent years, significant progress has been made in studying pore-scale multiple coupled reactive transport processes in CLs with realistic porous structures of CLs resolved [8,34]. To carry out pore-scale numerical studies of the reactive transport processes in CLs, one needs to answer three questions, which are in fact also the three key steps during the pore-scale numerical studies. First, how to precisely describe the realistic porous structures of CLs and detailed distributions of different constituents (carbon, Pt particle, electrolyte and pores)? Second, what multiple physicochemical processes inside CLs will be studied? Last but not least, what kind of numerical method will be adopted to solve the physicochemical processes? In the following sections, the three questions will be discussed, and existing answers in the literature as well as the answers in the present study will be introduced. The flowchart of structure reconstruction and numerical simulations are displayed in Fig. 2.

2.1. CL structure reconstruction

For pore-scale studies, the geometrical details of the porous media need to be defined *a priori* and serve as input for subsequent pore-scale modeling. CLs consist of four constituents including carbon, Pt, electrolyte and pore. Each constituent has distinct geometrical and physicochemical features, enabling multifunction of the CLs for different electrochemical reactive transport processes. Directly resolving structures and constituent distributions of CLs has been ongoing with the development of advanced experimental techniques such as X-ray, scanning electron microscope (SEM), transmission electron microscope (TEM), focused ion beam (FIB-SEM) and identical location (IL)-TEM. Combining several techniques which provide complementary information of CL structures is helpful for understanding the complete configuration of individual constituent inside CLs [35]. For example, very recently Nano-CT, small and ultra-small angle X-ray scattering, TEM and porosimetry were combined together to explore the agglomerate structures in CLs [36]. Agglomerate structures with resolution as high as 1 nm were reconstructed including primary and secondary pores, Pt particles, ionomer and carbon support. It was found that the agglomerate structures show high structural heterogeneities. The agglomerates present a wide size distribution from 50 nm to 600 nm, with 248 nm mean diameter and 104 nm standard deviation. The thickness of the ionomer film is spatially non-uniform and is strongly dependent on the I/C, which shows a wide distribution from 0 to 30 nm. Pt particles with highest diameter of about 10 nm were observed [36].

It is worth mentioning that direct high-resolution (nanometer scale) imaging of the 3D CL microstructure (especially the ionomer network) is still challenging [37,38]. Thus, reconstruction scheme plays an important role in obtaining CL structures, especially for the ionomer and Pt particles [15,36], and thus has been widely adopted in the literature. Based on previous 2D and 3D experimental images of CL structures and constituents, as well as previous reconstruction schemes in the literature, a reconstruction scheme for the four constituents in CL agglomerates was developed in our previous work [18,20]. The reconstruction is started within an empty domain, followed by adding different constituents sequentially.

Step 1: **carbon**. The constrained parameters for the reconstruction of carbon phase are carbon particle seed number N, diameter of carbon particles d, and the volume fraction of carbon phase ε_c. The reconstruction steps are as follows. (a) Based on ε_c and the size of the entire computational domain, the carbon seed number N is calculated, with the assumption that there are N carbon particles with diameter d randomly distributed in the domain. (b) The position of each carbon
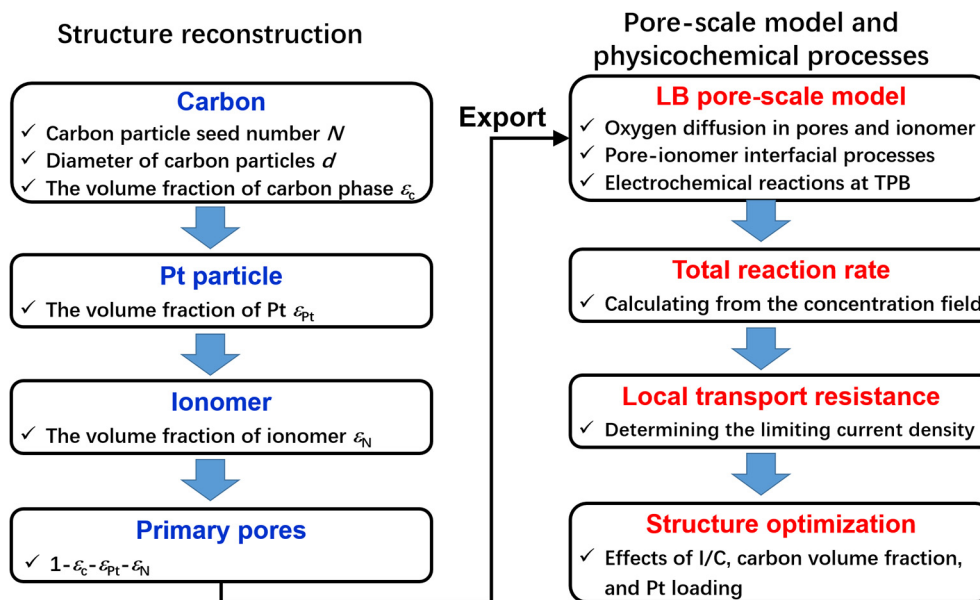
Structure reconstruction

Pore-scale model and physicochemical processes

Carbon
- ✓ Carbon particle seed number N
- ✓ Diameter of carbon particles d
- ✓ The volume fraction of carbon phase ε_c

Export

LB pore-scale model
- ✓ Oxygen diffusion in pores and ionomer
- ✓ Pore-ionomer interfacial processes
- ✓ Electrochemical reactions at TPB

Pt particle
- ✓ The volume fraction of Pt ε_{Pt}

Total reaction rate
- ✓ Calculating from the concentration field

Ionomer
- ✓ The volume fraction of ionomer ε_N

Local transport resistance
- ✓ Determining the limiting current density

Primary pores
- ✓ $1 - \varepsilon_c - \varepsilon_{Pt} - \varepsilon_N$

Structure optimization
- ✓ Effects of I/C, carbon volume fraction, and Pt loading

Fig. 2. Flowchart of the structure reconstruction scheme and pore-scale reactive transport model.

seed is randomly selected in the domain. These seeds are the nucleation sites for carbon particles; (c) For each seed, a solid sphere with diameter smaller than d is generated; (d) A scheme called quartet structure generation set (QSGS) is adopted to further grow each carbon particle until the prescribed ε_c is obtained. Note that on the one hand, directly growing carbon phase around carbon seeds without Step (c) was implemented in our previous work [18,20] as well as in that of Siddique and Liu [15]; on the other hand, carbon particle with diameter d is directly adopted in some reconstruction schemes [13,16]. Step (c) adopted here combines the above two schemes to consider both the sphere shape of carbon particles and the mushy zone at the outer surface between different carbon particles.

Step 2: **Pt**. Pt particles are randomly distributed on the surface of the carbon constituent already reconstructed in Step 1. The constrained variable for this step is the volume fraction of Pt particles ε_{Pt}. Note that the resolution of the reconstruction domain is 2 nm in the present study, which is the typical size of Pt particles identified in the literature [39,40]. Such resolution has been demonstrated to guarantee agreement between simulation and experimental results in our previous studies [20,41]. It is worth mentioning that experimental results show that Pt particles conform to a particle size distribution (PSD), and the PSD changes during Pt degradation. Effects of the PSD can not be neglected, and one can refer to Ref. [41] for more details. The emphasis of the present study is placed on effects of interfacial transport processes across interface of different constituents.

Step 3: **ionomer**. The least understood constituent in CLs is the ionomer phase, especially its 3D structures. Commonly used ionomer is Nafion. Advanced techniques, such as TEM, atomic force microscopy (AFM) and high-angle annular dark-field scanning TEM (HAADF-STEM), revealed that ionomer forms a thin film with thickness from a few nanometers to tens of nanometers covering on the surface of Pt/C [36–38]. Based on the above observation, two kinds of interfacial meshes are identified, one is that between Pt/C and unfilled meshes, and the other is that between ionomer and unfilled meshes. For each interfacial mesh belonging to the two kinds, a random number is generated. If the random number is smaller than a prescribed probability P which is far less than the volume fraction of ionomer ε_N, the mesh is set as ionomer phase. To guarantee the connectivity of ionomer phase, the probability P for the interfacial meshes between ionomer and unfilled meshes is higher than that between Pt/C and unfilled meshes [18].

Step 4: **Primary pore**. Through Steps 1–3, the domain is partially

filled with carbon, Pt and ionomer phase with prescribed volume fraction of each constituent. The remained space in the domain is thus the pores.

Important parameters describing the reconstructed structures include Pt to carbon weight ratio Pt/C, ionomer to carbon weight ratio I/C and Pt loading, which are calculated by

$$Pt/C = \frac{\rho_{Pt}V_{Pt}}{\rho\varepsilon_{Pt}V_{Pt} + \rho_c V_c} = \frac{\rho_{Pt}V\varepsilon_{Pt}}{\rho_{Pt}V\varepsilon_{Pt} + \rho_c V\varepsilon_c} \tag{1a}$$

$$I/C = \frac{\rho_N V_N}{\rho_N V_N + \rho_c V_c} = \frac{\rho_N V\varepsilon_N}{\rho_N V\varepsilon_N + \rho_c V\varepsilon_c} \tag{1b}$$

$$\gamma_{Pt} = \frac{\rho_{Pt}V_{Pt}}{V/(1 - \varepsilon_s)}L_{CL} \tag{1c}$$

where ρ and V are density and volume, respectively. The subscript "Pt", "C" and "N" denote Platinum, carbon and ionomer, respectively. L_{CL} is the CL thickness, and ε_s is the porosity of the secondary pores. The density is 21.45 g cm^{-3}, 1.8 g cm^{-3} and 2.0 g cm^{-3} for Pt, carbon and ionomer, respectively.

Fig. 3(a)–(c) shows a reconstructed 3D structure with carbon, Pt/C and thin ionomer film covered on the Pt/C, respectively. The domain is a spherical porous agglomerate with radius of 100 nm, the size of which is typical in CLs according to recent experimental results [35]. In Fig. 3(a)–(c), volume fraction of the carbon is 0.5, Pt loading is 0.2 mg cm^{-2}, I/C is 0.5 and the porosity is 0.21. It can be found that microscopic structures of carbon skeleton are quite complex, in agreement with the TEM images shown in Fig. 1(a). Nanoscale Pt particles are randomly distributed on the surface of carbon, and ionomer forms a thin film covering Pt/C. The thickness of ionomer film is not uniform, and there are a few Pt particles not covered by the ionomer which thus cannot be utilized. Fig. 3(d)–(f) further displays the reconstructed structures with different I/C. It can be observed that as I/C increases, more and more Pt/C are covered by the ionomer, while the pore volume decreases. For the case with I/C as 0.8, the pores inside the agglomerate are almost completely filled with ionomer. Fig. 4 further shows the ionomer thickness distribution for different I/C. It can be found that as I/C increases, the ionomer film becomes thicker. The typical thickness of the ionomer is from a few nanometers to tens of nanometers.
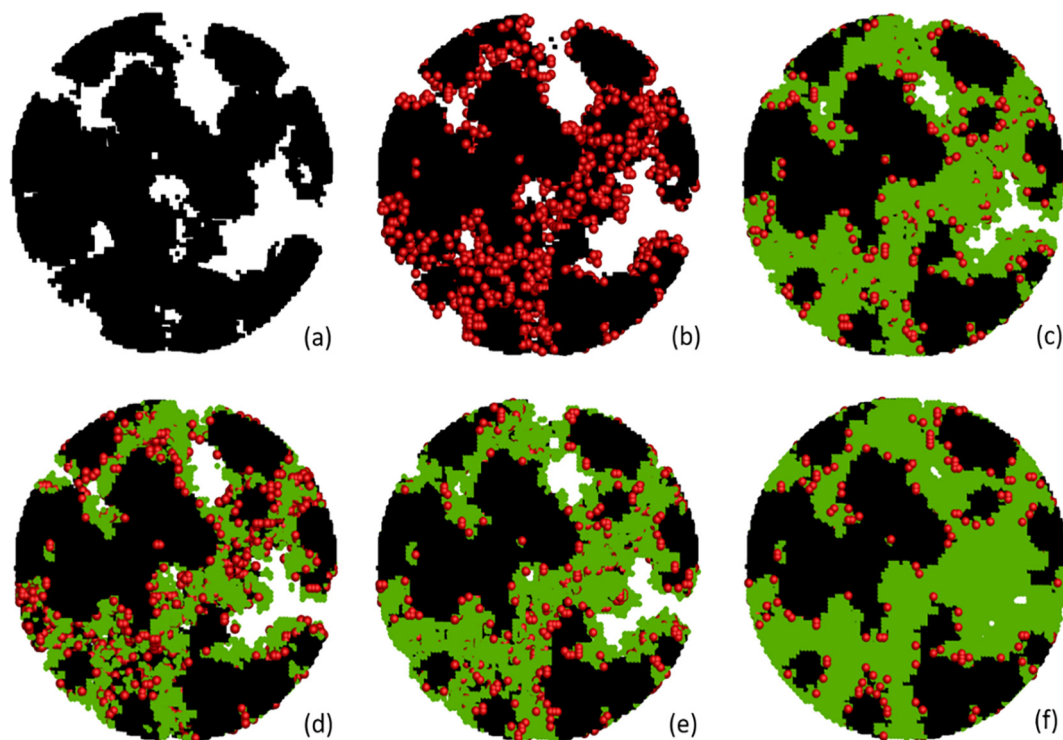
Fig. 3. Reconstructed structures of CL in PEMFC. (a)–(c) Reconstruction processes of different phases in CLs. (a) carbon phase, (b) Pt/C and (c) thin ionomer film covered on the Pt/C, respectively. In (c) I/C = 0.5. (d)–(f) CL structures with different I/C: (d) I/C = 0.2; (e) I/C = 0.4; and (f) I/C = 0.8. In all the images, volume fraction of carbon is 0.5 and Pt loading is 0.2 mg cm^{-2}. Black, red and green parts denote carbon, Pt particles and ionomer. (For interpretation of the references to colour in this figure legend, the reader is referred to the web version of this article.)
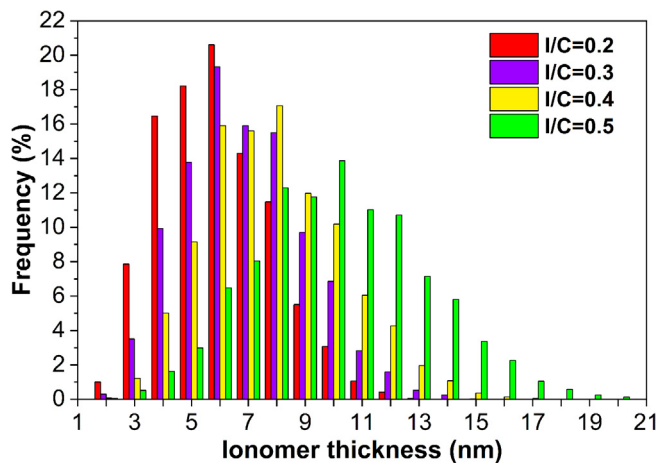
Fig. 4. Thickness distributions of ionomer film.

2.2. Physicochemical models

Fabricating CLs as nanoscale porous media greatly increases the specific surface area, which is desirable for obtaining more active sites. This, however, brings additional challenges for understanding the reactive transport processes inside the CLs. A lot of interface between different constituents exists in the porous CLs, leading to complex interfacial transport phenomena. Besides, heterogeneous electrochemical reaction takes place at the TPB. Currently, there are still remaining questions about reactive transport in CLs, such as the state and transport of water in the nanoscale confined space [21,22], and transport properties of the thin ionomer film [27,42]. Water in CLs plays multiple roles. On the one hand, water blocks the pores and thus hinders the transport of reactant gas [21], reducing the cell performance. On the other hand, liquid water in micropores can provide pathways for

proton, thus reducing the transport resistance of proton, which is desirable for the electrochemical reaction [43]. Therefore, effects of water on the reactive transport processes inside the CLs need further investigation.

In the present study, the physicochemical model established is based on the state-of-the-art understanding of pore-scale reactive transport processes within nanoscale confined space of CLs, especially the interfacial transport processes of oxygen across pore-ionomer interface recently identified under low Pt loading [28]. The pore-scale physicochemical processes studied are schematically shown in Fig. 1(b) and (c), including bulk transport of oxygen in pores and local reactive transport of oxygen in the thin ionomer film, respectively. To help understand the oxygen concentration variation during the reactive transport processes, Fig. 5 is displayed. The corresponding governing equations are as follows.

The oxygen first diffuses in the pores between carbon particles obeying the Fick law

$$\nabla(D_{\mathrm{p}} \nabla C_{\mathrm{g}}) = 0 \tag{2}$$

where C_{g} is the gas concentration. D_{p} is the diffusivity taking into account both bulk diffusion and Knudsen diffusion

$$D_{\mathrm{p}} = (D_{\mathrm{b}}^{-1} + D_{\mathrm{Kn}}^{-1})^{-1} \tag{3}$$

where the bulk diffusivity and Knudsen diffusivity are calculated by [44]

$$D_b = 0.22 \times 10^{-4} \frac{(T/293.2)^{1.5}}{P/101325}, \quad D_{Kn} = \frac{d_p}{3}\sqrt{\frac{8RT}{\pi M_{O_2}}} \tag{4}$$

where T and P are the temperature and pressure, respectively. R is the gas constant and M is the molar mass. d_{p} is the pore diameter. In the present study, the 13-direction averaging method is adopted to determine the local pore diameter of each void node [18]. Starting from a void node P, nodes in a given direction are visited until a non-pore node
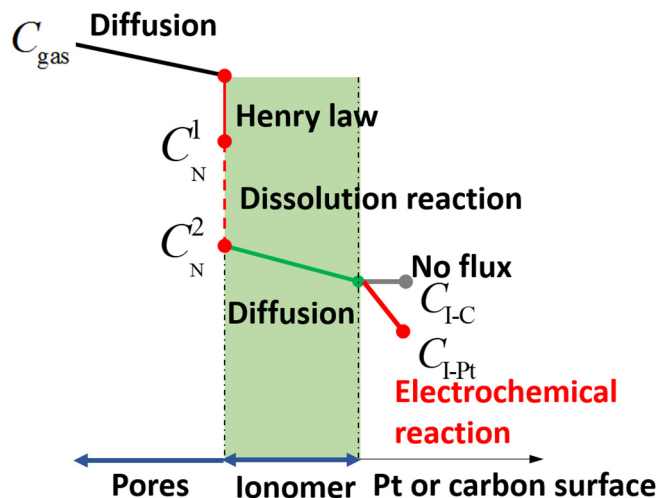
Fig. 5. Schematic of oxygen concentration variation during the reactive transport processes.

Q is reached, and the length is calculated between P and Q. The 13-directions visited include three directions along x, y and z axis, six diagonal directions in x-y, y-z and x-z plane, and four diagonal directions traversing the 3-D space. The local pore diameter is averaged values of the length in the 13-directions.

At the pore-ionomer interface, the concentration undergoes a drop due to the Henry law as follows

$$C_N^1 = \frac{C_g}{H} \tag{5}$$

where H is the Henry constant.

At the nanoscale the gas transport across the pore-ionomer interface is not in equilibrium, and the following interfacial dissolution reaction is considered [25,27–30]

$$D_p \frac{\partial C_g}{\partial n} = -k_{dis}(C_N^1 - C_N^2) = -\frac{1}{R_{int}}(C_N^1 - C_N^2) = D_N \frac{\partial C_N}{\partial n} \tag{6}$$

where k_{dis} is the dissolution reaction rate constant, R_{int} is the corresponding resistance and n is the normal direction of the interface. Recently, the k_{dis} with limited value has been found to be responsible for the widely observed extra transport resistance under low Pt loading [25,27–30].

Inside the ionomer, the dissolved oxygen diffuses according to the following equation

$$\nabla(D_N \nabla C_N) = 0 \tag{7}$$

where D_N is the diffusivity inside the ionomer.

There are possibly five kinds of interface in CLs as can be observed in Fig. 1. The transport process at the pore-ionomer (PI) interface is described by Eqs. (5) and (6). For the pore-carbon (PC) interface, pore-Pt (PP) interface, and ionomer-carbon (IC) interface, there is no chemical reaction and thus no-flux boundary is adopted locally. At the ionomer-Pt (IP) interface, electrochemical reaction occurs

$$D_N \frac{\partial C_N}{\partial n} = k_{elec} C_N \tag{8}$$

The chemical reaction coefficient k_{elec} is determined by the Butler-Volmer equation

$$k_{elec} = \frac{1}{4F} \frac{i_0^{ref}}{C_{O_2,ref}} \left[\exp(-\frac{\alpha_c F}{RT}\eta) - \exp(\frac{(1-\alpha_c)F}{RT}\eta) \right] \tag{9}$$

where F is the Faraday constant. i_0^{ref}, $C_{O_2,ref}$, α_c and η are the exchange current density, the reference concentration, the transfer coefficient and the overpotential respectively. In the present study, the Damkohler number Da is adopted to represent the relative strength between

electrochemical reaction and diffusion. The Da is defined as follows

$$Da = \frac{k_{elec}d}{D_p} \tag{10}$$

where d is the character length of the computational domain, choosing as the diameter of the agglomerates studied in the present study. With Eq. (10), Eq. (8) is modified as

$$\frac{\partial C_N}{\partial n} = \frac{Da}{d} C_N \tag{11}$$

From the above description, it can be found that the simulation of multiple physicochemical reaction in the cathode CL is a particularly challenging task. The major difficulty arises from the interfacial processes, especially the large variations of transport properties in the pores and the ionomer. First, there is a concentration drop across the pore-ionomer interface described by the Henry law (Eq. (5)) with Henry constant around 50. Second, the diffusivity of oxygen in the electrolyte is 4–5 orders of magnitude lower than that inside the pores. Third, the local non-equilibrium dissolution reaction takes place at the pore-electrolyte interface described by Eq. (6), the effects of which become prominent under lower Pt loading. To the best of our knowledge, there has been no pore-scale studies in the literature completely taking into account the discontinuous concentration, discontinuous diffusivity and the local dissolution reaction related to the pore-ionomer interfacial transport. In the present study, a 2D LB model recently developed by our group for interfacial transport with distinct transport properties [45] is further extended to 3D and is adopted to treat the pore-ionomer interfacial transport processes, which is introduced in the following section.

2.3. Numerical methods

Since the mid-1990s, the lattice Boltzmann method has gained a prominent role among the CFD approaches, due to its distinctive advantages such as intrinsic parallelization, easy implementation of boundary conditions in complex geometries [46]. The LBM provides an efficient tool for solving a wide class of transport processes especially for those in complex geometries such as porous media [46–48]. In the present study, the multi-relaxation-time (MRT) LB mass transport model is adopted, and the evolution equation of the concentration distribution function is as follows

$$g_i(\boldsymbol{x} + \boldsymbol{c}_i\Delta t, t + \Delta t) - g_i(\boldsymbol{x}, t) = \mathbf{Q}^{-1}\Lambda\mathbf{Q}(g_i(\boldsymbol{x}, t) - g_i^{eq}(\boldsymbol{x}, t)) \tag{12}$$

where g_i is the concentration distribution function at the lattice site x and time t in the ith direction. Δt is the time step and $\boldsymbol{c}_i$ is the lattice velocity. In the present study, D3Q7 lattice model is adopted and the corresponding $\boldsymbol{c}_i$ is as follows

$$\boldsymbol{c}_i = \begin{cases} 0 & i = 0 \\ (\pm 1, 0, 0), \ (0, \pm 1, 0), \ (0, \pm 1, 0) & i = 1\sim 6 \end{cases} \tag{13}$$

It is worth mentioning that while lattice model with more lattice velocities (such as D3Q15 and D3Q18) is required for modeling fluid flow, D3Q7 is sufficient for diffusion process as concentration is a scalar. In fact, the D3Q7 lattice model has been successfully adopted to accurately simulate a wide range of diffusion processes, and one can refer to these literatures for more details [20,33,49,50].

g_i^{eq} in Eq. (12) is the equilibrium distribution function

$$g_i^{eq} = w_i C, \ w_0 = \frac{1}{4}, \ w_{1-6} = \frac{1}{8}, \tag{14}$$

$\mathbf{Q}$ in Eq. (12) is the transformation matrix which transfers the distribution function in velocity space into momentum space

$$Q = \begin{bmatrix} 1, & 1, & 1, & 1, & 1, & 1, & 1 \\ 0, & 1, & -1, & 0, & 0, & 0, & 0 \\ 0, & 0, & 0, & 1, & -1, & 0, & 0 \\ 0, & 0, & 0, & 0, & 0, & 1, & -1 \\ 6, & -1, & -1, & -1, & -1, & -1, & -1 \\ 0, & 2, & 2, & -1, & -1, & -1, & -1 \\ 0, & 0, & 0, & 1, & 1, & -1, & -1 \end{bmatrix} \tag{15}$$

and Q^{-1} is inverse matrix of Q. The relaxation coefficient matrix$\Lambda$is as follows

$$\Lambda = \begin{bmatrix} \tau_0, & 0, & 0, & 0, & 0, & 0, & 0 \\ 0, & \tau_{xx}, & \tau_{xy}, & \tau_{xz}, & 0, & 0, & 0 \\ 0, & \tau_{yx}, & \tau_{yy}, & \tau_{yz}, & 0, & 0, & 0 \\ 0, & \tau_{zx}, & \tau_{zy}, & \tau_{zz}, & 0, & 0, & 0 \\ 0, & 0, & 0, & 0, & \tau_4, & 0, & 0 \\ 0, & 0, & 0, & 0, & 0, & \tau_5, & 0 \\ 0, & 0, & 0, & 0, & 0, & 0, & \tau_6 \end{bmatrix} \tag{16}$$

where $\tau_{\alpha\beta}$ is the relaxation coefficients. Its relationship with diffusivity is as follows

$$D_{\alpha\beta} = \zeta \left(\tau_{\alpha\beta} - \frac{1}{2}\delta_{\alpha\beta} \right) \frac{\Delta x^2}{\Delta t} \tag{17}$$

where $\delta_{\alpha\beta}$ is the kronecker symbol. For isotropic mass transport, $\tau_{xx} = \tau_{yy} = \tau_{zz}$ and $\tau_{\alpha\beta}(\alpha \neq \beta) = 0$. Besides, $\tau_0, \tau_4, \tau_5,$ and $\tau_6$in Eq. (16) are set as unity without loss of numerical stability. ζin Eq. (17) is set as $1/4$ in this study.

Now attention is turned to treatment of the pore-ionomer interfacial transport processes described by Eqs. (2)–(6) in the LB framework. It is worth mentioning that the interfacial transport processes with significant concentration jump, large diffusivity ratio and interfacial dissolution reaction pose a great challenge not only for the LBM, but also for traditional CFD methods such as FVM, FEM and FDM. Traditional CFD methods require corrections at the interface with extrapolations and iterative schemes. Due to its kinetic nature, the LBM is inherently superior to treat interface with complicated shapes [45]. In the LB framework, there are two key steps, namely Collision and Streaming, both of which are linear

Collision: $\quad \hat{g}_i(\boldsymbol{x}, t) = g_i(\boldsymbol{x}, t) - Q^{-1}\Lambda Q(g_i(\boldsymbol{x}, t) - g_i^{eq}(\boldsymbol{x}, t)) \tag{18a}$

Streaming: $\quad g_i(\boldsymbol{x} + \boldsymbol{c}_i\Delta t, t + \Delta t) = \hat{g}_i(\boldsymbol{x}, t) \tag{18b}$

where$\hat{g}_i$ is the distribution function after collision. The collision step is totally local as shown in Eq. (18a); however, the streaming step requires distribution functions from neighboring nodes. For example as shown in Fig. 6, for node A in the pore, when the streaming step is implemented, the distribution function g_i from its neighboring node B is required; however, node B belongs to the ionomer. Across the phase interface A and B, complicated interfacial transport processes occur. In our
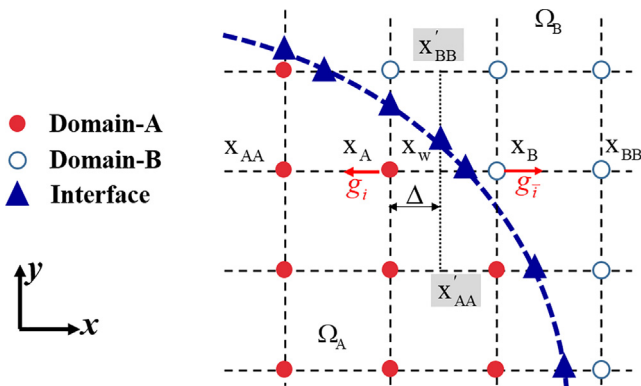

Fig. 6. Schematic of the interfacial nodes in the LB framework and the unknown distribution functions in different phases.

previous study, the following scheme is proposed for the unknown distribution functions of interfacial nodes A and B [45]

$$g_i(\mathbf{x}_A, t + \Delta t) = \frac{1}{-\frac{1}{k_{dis}}\zeta\frac{\Delta x}{\Delta t} - \frac{1}{H} - 1}\left[\left(-\frac{1}{k_{dis}}\zeta\frac{\Delta x}{\Delta t} + \frac{1}{H} - 1 \right)\hat{g}_i(\mathbf{x}_A, t) \right.$$
$$\left. - 2\hat{g}_{\bar{i}}(\mathbf{x}_B, t) \right]$$

$$g_{\bar{i}}(\mathbf{x}_B, t + \Delta t) = \frac{1}{-\frac{1}{k_{dis}}\zeta\frac{\Delta x}{\Delta t} - \frac{1}{H} - 1}\left[\left(-\frac{1}{k_{dis}}\zeta\frac{\Delta x}{\Delta t} - \frac{1}{H} + 1 \right)\hat{g}_{\bar{i}}(\mathbf{x}_B, t) \right.$$
$$\left. - \frac{2}{H}\hat{g}_{\bar{i}}(\mathbf{x}_A, t) \right] \tag{19}$$

The unknown distribution functions at the left side of Eq. (19) are related to the known distribution functions$\hat{g}_i$at the right side as well as the Henry constant H and the dissolution reaction rate constant k_{dis}. Note that the large ratio of diffusivity in the two phases are accounted for in Eq. (17) by setting different values of $\tau_{\alpha\beta}$corresponding to different diffusivity. For more details of Eq. (19), one can refer to our previous work [45].

In LBM simulations, the variables are in lattice units instead of physical units. To implement the LB model it is necessary to obtain a consistent set of parameters that correspond to the physical parameters for the problem at hand. This is achieved by equating various dimensionless groups. For diffusivity

$$\frac{D_P}{\Delta x_P^2/\Delta t_P} = \frac{D_L}{\Delta x_L^2/\Delta t_L} \tag{20}$$

with subscript "P" and "L" representing "physical units" and "lattice units", respectively. Δx_L and Δt_L equal unity in the LBM. After the computational domain is defined and discretized, the physical length of a lattice Δx_P can be determined which is 2 nm in the present study. Other variables in physical units, such as reaction rate coefficient k_{elec} in Eq. (8), can be calculated from their corresponding one in lattice units by matching the dimensionless number

$$\frac{k_{elec,P}l_P}{D_P} = \frac{k_{elec,L}l_L}{D_L} \tag{21}$$

For dimensionless variable such as the Henry constant in Eq. (5), the value in the LB units is the same as that in the physical units.

In the following section, the LB model developed above is adopted to solve the reactive transport processes described in Section 2.2. Effects of the interfacial phenomena on reactive transport processes in CLs are discussed in detail.

3. Results and discussions

3.1. Across pore-ionomer interface mass transport

First, a 3D diffusion process in a cubic domain is studied. The side length of the domain is 20 nm. The left half of the domain is pore, while the right half is filled with ionomer, leading to a sharp interface between the pore and ionomer. Diffusivity in the pore is $D_P = 4.0 \times 10^{-6}$ m^2 s^{-1}, a typical value of diffusivity in the nanoscale pores [18]. For all the simulations, $\Delta x^2/\Delta t$in the LB is set as 1.6×10^{-6}. Therefore, according to Eq. (17), the collision time in the pore is 10.5. Diffusivity inside the ionomer is varied to test the capacity of the LB model developed. For example, for diffusivity in the ionomer as 8.0×10^{-10} m^2 s^{-1}, the collision time is 0.502. The boundary conditions are as follows. At the left inlet and right outlet, oxygen concentration is prescribed as C_0 and C_1, respectively. For the other four boundaries, periodic boundary conditions are adopted. This process is actually a 1D problem as schematically shown in Fig. 7(a) with following analytical solution
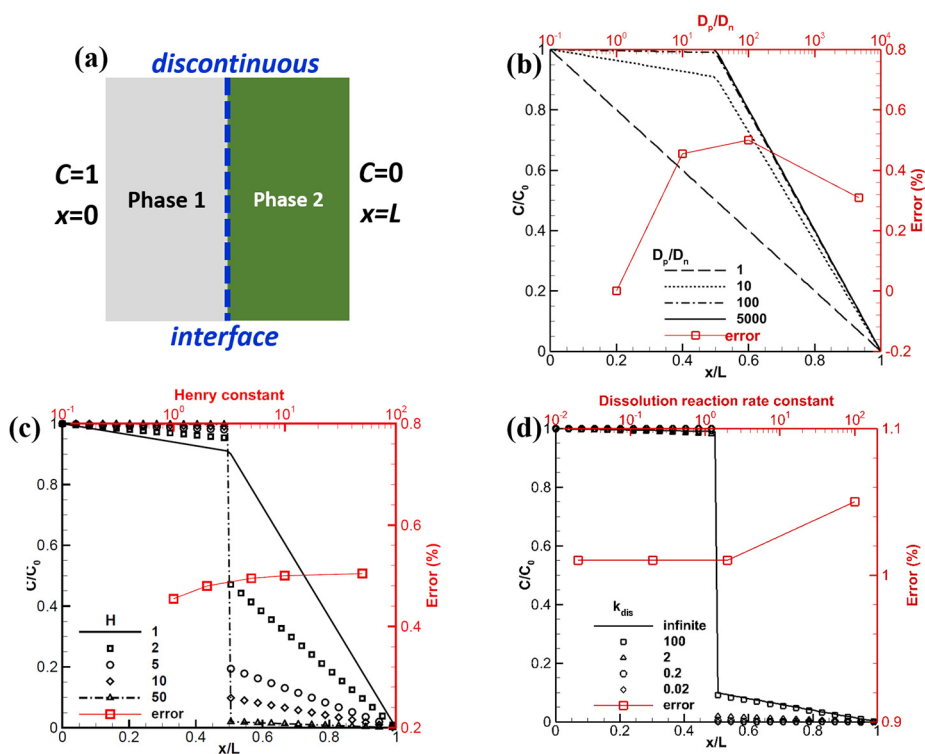
Fig. 7. Across pore-ionomer interface diffusion process in a cubic domain, in which left and right half are void space and ionomer, respectively. (a) schematic of the across-phase interface diffusion problem studied, (b) diffusion process under different diffusivity ratio, (c) diffusion with concentration drop at the phase interface considered, $D_P/D_N = 10$ and (d) diffusion with dissolution resistance at the phase interface further considered, $D_P/D_N = 10$ and $H = 10$. Relative error between LB simulated results and analytical solution is also plotted.

$$\begin{cases} C_x = C_0 - (C_0 - C_{g,\,x=0.5L})\dfrac{x}{0.5L} & 0 \leqslant x < 0.5L \\ C_x = C_{N,\,x=0.5L}\dfrac{L-x}{0.5L} & 0.5L \leqslant x \leqslant L \end{cases} \tag{22}$$

where $C_{g,\,x=0.5L}$ and $C_{N,\,x=0.5L}$ are the gas concentration on the pore and ionomer side of the phase interface, respectively

$$C_{g,\,x=0.5L} = \frac{D_P/0.5L + D_P k_{dis}/D_N}{D_P/0.5L + k_{dis}/H + D_P k_{dis}/D_N} C_0$$

$$C_{N,\,x=0.5L} = \frac{D_P}{D_N}\left(\frac{k_{dis}/H}{D_P/0.5L + k_{dis}/H + D_P k_{dis}/D_N}\right) C_0 \tag{23}$$

First, the diffusion process with H as 1 and infinite k_{dis} is studied. Infinite k_{dis} indicates that there is no dissolution resistance at the pore-ionomer interface. The domain is discretized using 20*20*20 lattices, thus the resolution is 1 nm/lattice. Fig. 7(b) shows the results for the concentration along x direction under different D_P/D_N, where D_P is constant as 4.0×10^{-6} m² s⁻¹. For $D_P/D_N = 1$, the concertation distribution is linear, as expected. As D_P/D_N increases, a turning point appears at the phase interface ($x/L = 0.5$), leading to different slope of the linear distributions at each side of the phase interface. It can be found that the higher the D_P/D_N, the higher the value of the concentration at the turning point, indicating reduced diffusion flux which is calculated by $D\Delta C$ in each constituent. Fig. 7(b) also shows the relative error between the simulated results and analytical solutions given by Eq. (22). The error is below 0.5% even for the case with D_g/D_N as high as 5000, indicating strong capacity of the 3D LB model developed for predicting mass transport process across constituent interface with high diffusivity ratio.

Second, concentration drop across the interface obeying the Henry law is considered, while the dissolution resistance is still not considered with infinite k_{dis}. Fig. 7(c) shows the concentration distribution along x direction with different Henry constant, in which D_P/D_N is 10. As shown in Fig. 7(c), the gas concentration is not continuous across the interface, as expected according to the Henry law. Increasing H also leads to reduced diffusion flux. The relative error between the simulated and analytical concentrations is also plotted. It can be found that the relative error is below 0.5% even for the case with Henry constant as 50, further demonstrating the accuracy of the 3D LB model developed for

mass transport across phase interface with concentration jump.

Finally, transport processes with all the interfacial phenomena are simulated, including large diffusivity ratio, concentration drop (Henry Law) and interfacial dissolution reaction. Fig. 7(d) shows the concentration distributions under different k_{dis}, where H is 10 and D_P/D_N is 10. It can be found that as k_{dis} decreases, namely the dissolution resistance across the interface becomes higher, the concentration drop across the interface becomes more significant. For k_{dis} as 0.02 (lattice units), gas concentration at the ionomer side of the interface is as low as 2.49×10^{-4} (the analytical solution is 2.46×10^{-4}). Such result indicates that the dissolution resistance across the pore-ionomer phase should be as low as possible, otherwise it will cause severe concentration polarization in PEMFCs. The numerical results are also compared with the analytical solutions, and good agreement is obtained again.

3.2. Across pore-ionomer interface mass transport with reaction

Now attention is turned to study electrochemical reactive transport in a simple yet typical local CL structure consisting of pore, electrolyte and reactive sites (Pt/C in PEMFC), as schematically shown in Fig. 8(a). The width for the pore and electrolyte is 14 and 6 nm, respectively. Oxygen diffuses in the pores, dissolves at the pore-ionomer interface, transfers inside the electrolyte, and finally reacts at the reactive surface at the right boundary. At $x = 0$, concentration of oxygen is prescribed as C_0. At $x = L$, namely, the reactive surface, electrochemical reactions described by Eq. (8) take place. For the y and z directions, periodic boundary conditions are adopted. The domain size is 20*20*20 lattices. The LB developed in Section 2.3 is applied for the above electrochemical reaction processes at the triple-phase boundary. Fig. 8(b) shows the relationship between total reaction rate ψ and Da number, where the total reaction rate is the summation of kC_s over all the reaction sites. ψ first increases quickly with Da and finally approaches a maximum value ψ_{max}. ψ_{max} corresponds to the diffusion-controlled reactive transport region. It can be seen that with the actual diffusivity considered, ψ_{max} reduces from 216.2 to 0.16, which further drops to 3.72×10^{-3} and 1.48×10^{-3} with Henry law (H as 43) and pore-electrolyte interface dissolution resistance considered ($k_{dis} = 0.1$ or

(a)

(b)
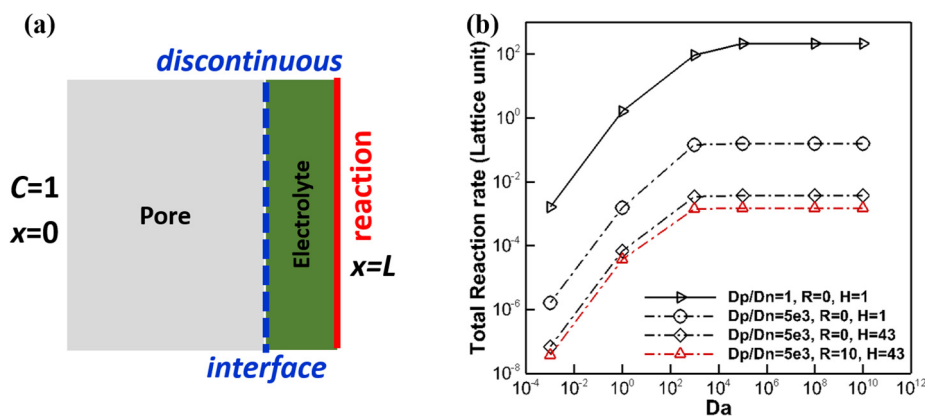
Fig. 8. Across-phase interface diffusion process in a cubic domain with electrochemical reaction. (a) Schematic of the across-phase interface diffusion process with electrochemical reaction studied, (b) relationship between Da number and the total reaction rate.

$R = 10$). With all the interfacial transport processes considered, ψ_{max} is five orders of magnitude lower than case with the interfacial transport processes neglected. This is because the gas transporting to the triple-phase boundary is greatly reduced by the slow diffusivity, low solubility and interfacial dissolution resistance in the ionomer.

3.3. Reactive transport in 3D porous structures of catalyst layers

Now attention is turned to the emphasis of the present study, the electrochemical reactive transport processes inside the nanoscale structures of CLs reconstructed in Section 2.1. It is commonly observed in experiments that carbon particles form agglomerates in CLs. Gas first diffuses in secondary pores between agglomerates, and then transports in primary pores inside the agglomerates. It has been demonstrated that the potential drop inside an agglomerate of typical size is small and can be ignored [43], and thus proton transport inside the agglomerate is not considered. This indicates constant overpotential in an agglomerate. Therefore, only oxygen transport and chemical reaction inside the agglomerates is studied, and the corresponding physicochemical model has been introduced in Section 2.2.

First, the relationship between Da and total reaction rate ψ under different interfacial reactive transport conditions are studied. It is found that as the actual diffusivity inside the ionomer is considered ($D_p/D_N = 5000$), ψ decreases by three orders of magnitude, which further greatly decreases by five orders of magnitude with all the interfacial reactive transport processes taking into account, in agreement with the results in Fig. 8. The results are not plotted here for brevity. In all the following results, the actual interfacial transport conditions are taken into account with H as 43, D_p/D_N as 5000 and k_{dis} as 0.1 [33].

3.3.1. Oxygen distribution

Fig. 9 shows the oxygen concentration distribution at the center of z axis inside the CLs with different I/C and Pt loading, in which the volume fraction of carbon is fixed as 0.5. In Fig. 9, the black part is carbon and the red dots are Pt particles. The agglomerate diameter is 200 nm. For all the simulations below, without special statement, Da is 1.0×10^3. With i_0^{ref}, $C_{O_2,ref}$, α_c and T as 0.01 A m^{-2}, 40.96 mol m^{-3}, 0.61 and 313 K, the corresponding overpotential η is 1.1 V based on Eqs. (8) and (9).

Note that concentration drop across the pore-ionomer interface is huge due to the considerable local transport resistance across the pore-ionomer interface. The concentration inside the pore is quite close to the inlet concentration C_0, while that in the ionomer is several orders of magnitude lower. Therefore, to more clearly display the oxygen concentration distributions, the concentration inside the pores (the white regions in Fig. 9) is blanked, and only oxygen concentration inside the ionomer is plotted. It can be found that as Pt loading increases, oxygen

concentration inside the ionomer decreases. Besides, as I/C increases, more regions are occupied by ionomer, leading to expanded regions with lower oxygen concentration. Note that to avoid the effects of randomness, the same structure of carbon is adopted when investigating effects of I/C or Pt loading, as shown in Fig. 9.

3.3.2. Total reaction rate

The total reaction rate per volume ψ [mol m^{-3} s^{-1}], or volumetric reaction rate, is defined as the total reaction rate at the surface of all the reactive sites (Pt particle surface) divided by the total volume. It is calculated as follows based on the final concentration field obtained from the pore-scale simulations

$$\psi = \frac{\sum k_{elec} C_s \bar{A}}{V} = \frac{i_V}{4F} \quad (24)$$

where C_s is the surface concentration at reactive sites, $\bar{A}$ is the reactive surface area of each reactive site and i_V is the volumetric current density. Fig. 10 displays effects of Pt loading on ψ for different values of I/C, in which the volume fraction of carbon is 0.5. It can be found that in Fig. 10(a)–(c) that as Pt loading decreases from 0.4 mg cm^{-2} to 0.025 mg cm^{-2}, ψ also decreases under the same Da. The insert images in Fig. 10(a)–(c) clearly display the maximum total reaction rate ψ_{max} obtained under extremely high Da. It is worth mentioning that ψ_{max} corresponds to the limiting current density, namely the maximum current density obtained. For I/C as 0.2, ψ_{max} is about 0.138 for Pt loading as 0.4 mg cm^{-2}, while that for Pt loading as 0.025 mg cm^{-2} is reduced by 55.9% to 0.0061. For I/C as 0.4 and 0.8, the reduction ratio is about 34.4% and 42.9%, respectively. It is worth mentioning that the CL porous structures generated by the reconstruction scheme are random, and thus effects of structure randomness on the total reactive rate should be explored. Additional numerical simulations are conducted on five agglomerate structures reconstructed from the same set of parameters, namely $\varepsilon_C = 0.5$, I/C = 0.4 and $\gamma_{Pt} = 0.4$ mg cm^{-2}. During the reconstruction, the solid structures of the carbon phase are fixed, and only distributions of ionomer and Pt particles are changed. ψ of the five structures are evaluated, and the relative error of ψ is less than 1%. Another case with lower Pt loading is also studied, with $\varepsilon_C = 0.5$, I/C = 0.4 and $\gamma_{Pt} = 0.25$ mg cm^{-2}. Five structures are reconstructed and the relative error of ψ is also less than 1%.

Recently as demonstrated by several studies in the literature, conventional agglomerate models widely adopted in the literature predict the same limiting current density, even if the Pt loading is greatly decreased [20,33,51,52]. This is because in the conventional agglomerate model, the assumption of homogenous mixture of carbon, Pt, pore and ionomer is adopted in the agglomerate core. Thus once the oxygen diffuses into the agglomerate core, electrochemical reaction takes place at every site. However, in practical CLs, Pt particles are randomly
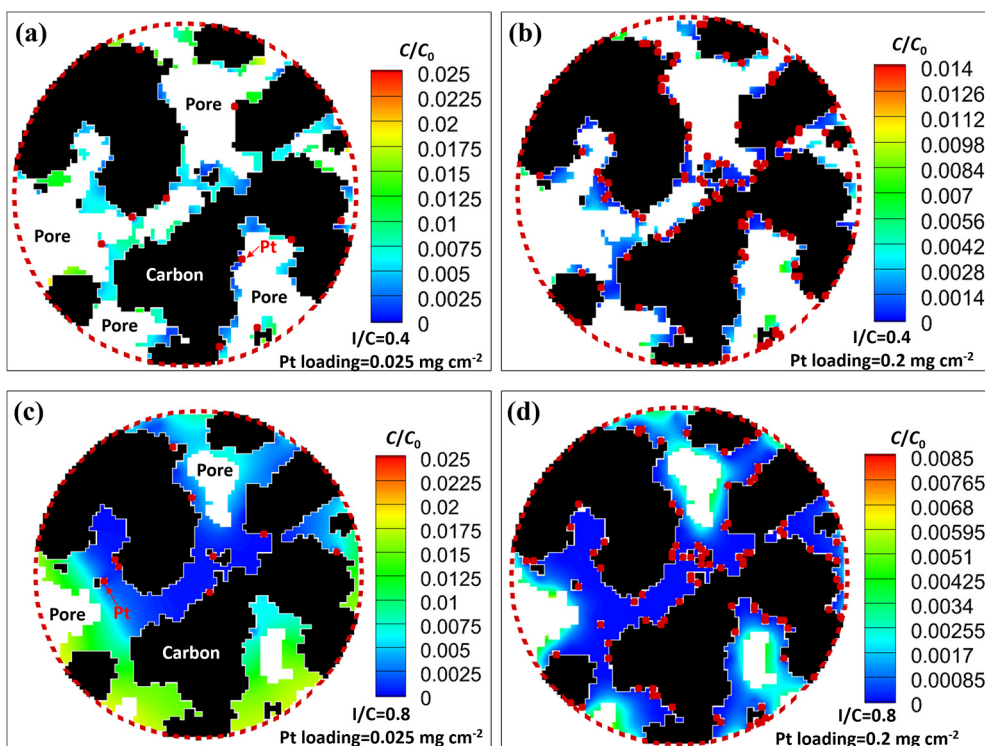
Fig. 9. Oxygen concentration contours under different Pt loading and I/C. (a) I/C = 0.4, Pt loading = 0.025 mg cm^{-2}, (b) I/C = 0.4, Pt loading = 0.2 mg cm^{-2}, (c) I/C = 0.8, Pt loading = 0.025 mg cm^{-2}, (d) I/C = 0.8, Pt loading = 0.2 mg cm^{-2}. The volume fraction of carbon is 0.5.

dispersed and reactive sites are limited especially under low Pt loading. Oxygen has to transport a certain distance before arriving at the reactive sites. Therefore, the conventional agglomerate model cannot accurately predict transport resistance inside the agglomerate core, and the error becomes significant under low Pt loading. By comparison, the porous agglomerate structure adopted in the present study directly

accounts for the details of Pt distribution inside CLs, thus successfully capturing the local transport resistance.

Maintaining the cell performance when Pt loading is reduced is highly desirable, leading to both good performance and low cost of PEMFC. Fig. 10(d) shows the reduction of ψ when Pt loading decreases from 0.4 mg cm^{-2} to 0.025 mg cm^{-2}. As shown in Fig. 10(d), there is
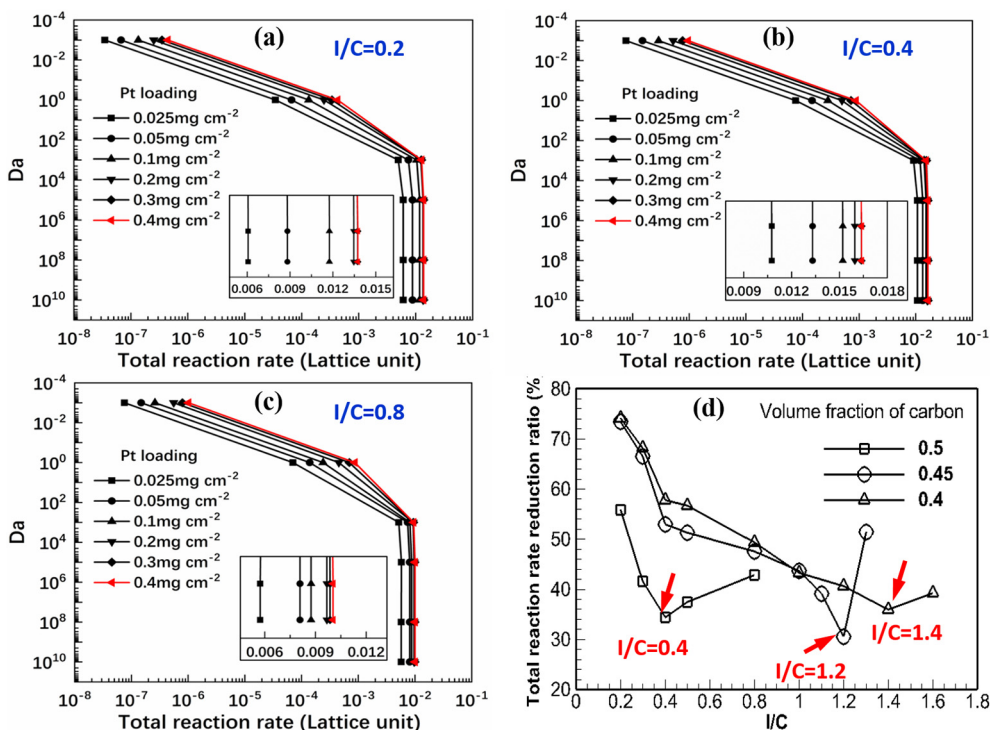

Fig. 10. Effects of Pt loading on total reaction rate. I/C is 0.2, 0.4 and 0.8 for (a)–(c) respectively. In (a)–(c), volume fraction of carbon is 0.5. (d) The reduction of the maximum total reaction rate when Pt loading is reduced from 0.4 mg cm^{-2} to 0.025 mg cm^{-2}.
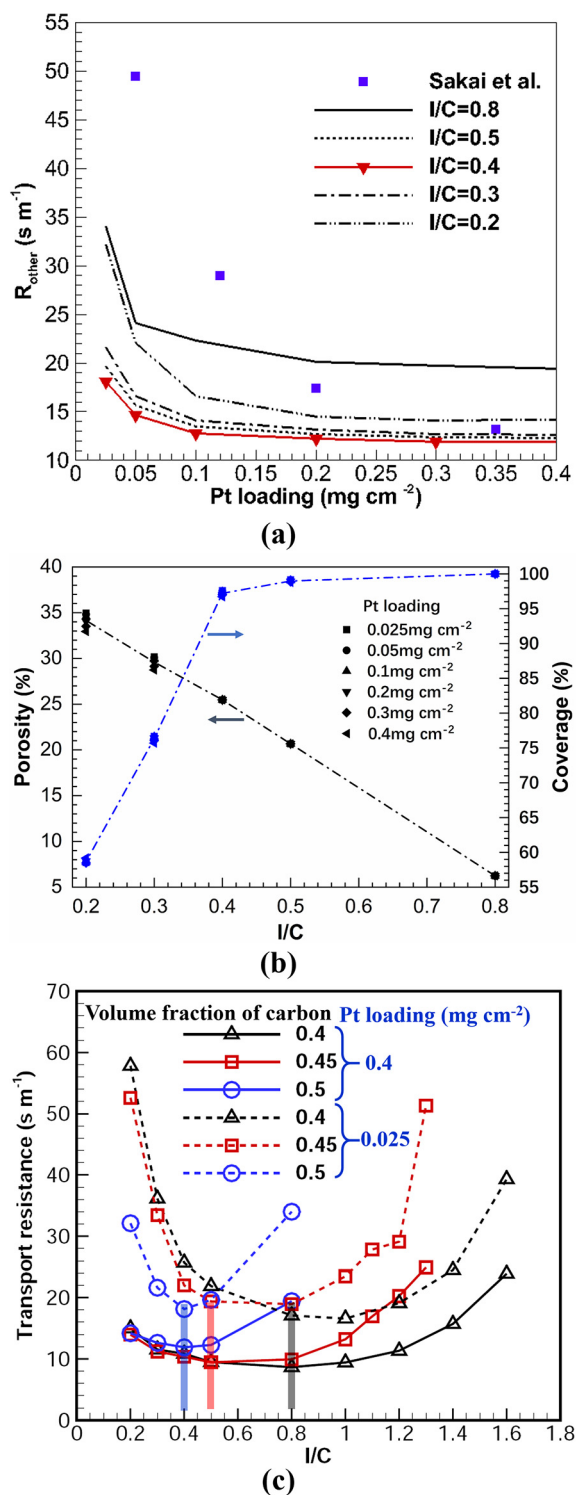
(a)

(b)

(c)

Fig. 11. Effects of Pt loading and I/C on the reactive transport processes in CLs. (a) local transport resistance. (b) porosity of primary pores and coverage ratio of Pt particles. (c) Effects of I/C on the local transport resistance under different volume fraction of carbon.

an optimum ionomer content which leads to the lowest performance loss, $(I/C)_{o,pl}$. $(I/C)_{o,pl}$ is 0.4, 1.2 and 1.4 for $\varepsilon_C = 0.5$, 0.45 and 0.4 respectively. The value of the optimum ionomer content increases as the volume fraction of the carbon phase decreases. This result will be discussed further in the following section.

3.3.3. Transport resistance

Finally, Fig. 11(a) shows the local transport resistance variation with Pt loading for different I/C. The local transport resistance is defined by the following equation [33]

$$R_{O_2} = \frac{C_{O_2}}{I_{lim}/nF}, \quad I_{lim} = nF\frac{\psi_{max}}{V/(1-\varepsilon_s)}L_{CL} \quad (25)$$

where C_{O_2} is the oxygen concentration supplied at the outer surface of the porous agglomerates reconstructed. I_{lim} is the limiting current density corresponding to the maximum total reaction rate ψ_{max}.

A lower transport resistance means a higher limiting current density. It can be found that for the same I/C, the transport resistance increases nonlinearly as the Pt loading decreases. The extra transport resistance is due to the interfacial transport resistance, which plays a prominent role particularly under low Pt loading. The results are in acceptable agreement with the experimental results of Sakai et al. [27]. An important observation from Fig. 11(a) is that as I/C decreases from 0.8 to 0.2, the local transport resistance firstly decreases, and then increases again. The value of I/C that leads to the lowest transport resistance is 0.4. To explain such result, Fig. 11(b) is provided which shows the effects of I/C on porosity of the primary pores ε_p and the coverage ratio of Pt particles ϖ in the reconstructed structures. It can be found that as I/C increases, ε_p decreases while ϖ increases. On the one hand, from the perspective of oxygen transport, lower I/C is desirable, because transport resistance at the pore-ionomer as well as that inside the ionomer is significantly higher than that in the pores. On the other hand, from the perspective of reactive sites, higher I/C is required, which leads to more Pt particles covered by the ionomer and thus high utilization of Pt particles. Therefore, there exists an optimized ionomer content in CLs, agreeing with the results in Fig. 11(a). Note that density of Pt is high, thus for the current Pt loading adopted in the CLs the volume fraction of Pt is quite low. Therefore, the Pt loading has negligible effects on the porosity. Besides, since the Pt particles are randomly and uniformly distributed inside the CLs, the coverage of Pt particles does not change as Pt loading varies.

Fig. 11(c) further shows the relationship between I/C and the transport resistance under different volume fraction of carbon. First, for the same volume fraction of carbon ε_c, the value of the optimum I/C leading to the lowest transport resistance, $(I/C)_{o,tr}$, is almost the same under different Pt loading. For example at $\varepsilon_c = 0.5$, $(I/C)_{o,tr}$ is 0.4, the same for the two Pt loadings. This result indicates that the Pt loading has negligible effects on $(I/C)_{o,tr}$. Second, as ε_c decreases, the value of $(I/C)_{o,tr}$ increases. The corresponding value of $(I/C)_{o,tr}$ is 0.4, 0.5, and 0.8 for ε_c as 0.5, 0.45 and 0.4, respectively. This is explained as follows. Considering a spherical carbon sphere with radius r covered by a thin ionomer film with thickness δ, I/C is calculated as follows

$$I/C = \frac{\rho_N\left(\frac{4}{3}\pi(r+\delta)^3 - \frac{4}{3}\pi r^3\right)}{\rho_C\frac{4}{3}\pi r^3} = \frac{\rho_N}{\rho_C}\left(\left(1+\frac{\delta}{r}\right)^3 - 1\right) \quad (26)$$

It can be found from Eq. (26) that as r decreases or the volume of carbon decreases, I/C increases.

In the literature, existence of optimum ionomer content has also been reported. The optimized ionomer content is generally expressed in the following three ways, the volume fraction of ionomer in CLs, the ionomer loading mg cm^{-2} (dry weight of ionomer divided by the geometrical area of CLs), and the weight percentage of ionomer wt. % (weight of ionomer to the total weight of CL). For the results obtained from our pore-scale simulations, the optimum value of ionomer content expressed in above three ways are listed in Table 1.

Using a 2D agglomerate model, Sun et al. [53] found the optimized ionomer volume fraction in CLs is about 0.48 for volume fraction of solid phase at 0.45. Antolini et al. [54] performed electrochemical studies using half-cell on electrodes with different ionomer contents, and found that the optimized ionomer content is 0.67 mg cm^{-2}. Antolini et al. also proposed an empirical equation to calculate the

Table 1
Optimum value of ionomer content in local structures of CLs.

Volume fraction of Carbon	0.5	0.45	0.4
Optimum I/C	0.4	0.5	0.8
a. Optimum volume fraction of Ionomer	0.192	0.203	0.288
b. Optimum ionomer weight ratio			
Pt loading: 0.4 mg cm^{-2}	0.164	0.186	0.262
Pt loading: 0.1 mg cm^{-2}	0.258	0.300	0.393
Pt loading: 0.025 mg cm^{-2}	0.292	0.337	0.441
c. Ionomer loading (mg cm^{-2})	0.19	0.20	0.29

optimum ionomer loading based on the Pt loading and Pt/C weight ratio, leading to the optimized ionomer weight percentage constant as 36 wt%. Sakikumar et al. [55] found that the optimum ionomer content depends on the platinum loading. For electrodes with different platinum loadings of 0.5, 0.25 and 0.1 mg cm^{-2}, the best performance is obtained at 20, 40 and 50 wt% of ionomer, respectively. As can be seen from Table 1, the optimum volume fraction of ionomer and ionomer loading do not depend on the Pt loading, while the optimum ionomer weight ratio decreases as the Pt loading increases for the same volume fraction of carbon, all of which are expected based on their definitions.

Results obtained in this study is in qualitative agreement with the above experimental results. However, quantitative comparison is currently not feasible yet. This is because the optimum value in the present study is for the local structures of CLs, namely that inside the porous agglomerates. Between different agglomerates, additional ionomer is also required for connecting different agglomerates, which will lead to higher optimum value in the entire CLs. This is the case in Table 1 where all the optimum values from the pore-scale simulations are lower than that in the experiments. In our group, a multiscale model is undergoing development which couples the pore-scale model in the present study with a cell-scale model. It is believed that the multiscale model with pore-scale processes incorporated will predict more accurately the transport processes in PEMFCs, and thus may be more powerful to find the optimal contents of different constituents in CLs. Once the multiscale model is fully developed, quantitative comparisons between the simulations and the experimental results will be possible.

Finally, as discussed in Fig. 10(d), there is an optimum ionomer content (I/C)$_{o,pl}$ which generates the lowest loss of cell performance when Pt loading is reduced. By comparing Fig. 10(d) with Fig. 11(c), it can be found that as volume fraction of carbon decreases, the value of (I/C)$_{o,pl}$ as well as that of (I/C)$_{o,tp}$ increase. However, the two values are generally different. For example, under volume fraction of carbon as 0.4, (I/C)$_{o,pl}$ is 1.4, while (I/C)$_{o,tp}$ is 0.8. The results indicate that the underlying transport processes in CLs are extremely complex, and it is challenging to achieve CL structures that leading to both high cell performance and the lowest performance loss under low Pt loading.

4. Conclusion

The CL is the key component of proton exchange membrane fuel cells in which the chemical energy is converted into electricity. Fabricating catalyst layers as multiphase materials enables multifunction for different electrochemical reactive transport processes. The state-of-the-art CL consists of four constituents including carbon, Pt, electrolyte and pore. Each constituent has distinct geometrical and physicochemical features. Coupled multiple reactive transport processes simultaneously occur in the complex porous structures of CLs, including oxygen diffusion in both pores and ionomer, electron transport in carbon phase, proton migration in ionomer and electrochemical reaction at the TPB. The nanoscale and multiphase characteristics of CLs bring challenges for understanding the reactive transport processes inside catalyst layers. Multiple constituent interface and interfacial transport exist in the porous CLs. Across the pore-ionomer interface, oxygen transport process is characterized by Henry's law, large diffusivity ratio, and interfacial non-equilibrium dissolution reaction,

leading to considerable concentration drop across the pore-ionomer interface. Understanding such pore-ionomer interfacial transport process and its effect on the cell performance is crucial for optimizing the CL structures, improving cell performance and reducing the cost.

In this study, a pore-scale model is developed to fully account for the reactive transport processes in local structures of CLs including oxygen diffusion in both pores and ionomer, oxygen across pore-ionomer interface transport and the electrochemical reaction at the TPB. The pore-scale model includes: a) a reconstruction scheme for porous structures of CLs with different Pt loading and I/C, in which all the four constituents of CLs are resolved with resolution as high as 2 nm; b) the physicochemical model describing oxygen reactive transport processes with the interfacial processes particularly considered; and c) the numerical method solving the complex reactive transport processes using the LBM. The pore-scale model is validated by 1D across phase interface transport processes with Henry constant as high as 50, diffusivity ratio as high as 5000, and interfacial dissolution reaction with reaction rate constant as low as 0.02. Pore-scale simulations are then conducted to study reactive transport processes inside the complex porous structures of CLs. The main conclusions are as follows:

(1) The total reaction rate or the limiting current density is significantly reduced by the interfacial reactive transport processes.
(2) The pore-scale model successfully predicts the physical results that limiting current density decreases with the decreases of the Pt loading, while the widely adopted agglomerate model fails to. For example, for I/C as 0.2 and volume fraction of carbon as 0.5, the limiting current density is reduced by 55.9% when Pt loading is reduced from 0.4 mg cm^{-2} to 0.025 mg cm^{-2}.
(3) There also exists an optimum ionomer content (I/C)$_{o,pl}$ which leads to the lowest performance loss when Pt loading is reduced. (I/C)$_{o,pl}$ is 0.4, 1.2 and 1.4 for ε_C = 0.5, 0.45 and 0.4 respectively.
(4) There is an optimum ionomer content (I/C)$_{o,tr}$ which leas to lowest oxygen transport resistance. (I/C)$_{o,tr}$ increases as the volume fraction of carbon decreases. (I/C)$_{o,tr}$ is 0.4, 0.5 and 0.8 for ε_C = 0.5, 0.45 and 0.4 respectively.
(5) The values of (I/C)$_{o,tr}$ and (I/C)$_{o,pl}$ generally are different, indicating it is challenging to achieve both the highest cell performance and the lowest performance loss as Pt loading decreases.

Declaration of Competing Interest

The authors declare that they have no known competing financial interests or personal relationships that could have appeared to influence the work reported in this paper.

References

[1] J.-H. Wee, K.-Y. Lee, S.H. Kim, Fabrication methods for low-Pt-loading electrocatalysts in proton exchange membrane fuel cell systems, J. Power Sources 165 (2007) 667–677.
[2] A.Z. Weber, J. Newman, Modeling transport in polymer-electrolyte fuel cells, Chem. Rev. 104 (2004) 4679–4726.
[3] G.R. Molaeimanesh, H. Saeidi Googarchin, A. Qasemian Moqaddam, Lattice Boltzmann simulation of proton exchange membrane fuel cells – a review on opportunities and challenges, Int. J. Hydrogen Energy 41 (2016) 22221–22245.
[4] T. Berning, D.M. Lu, N. Djilali, Three-dimensional computational analysis of transport phenomena in a PEM fuel cell, J. Power Sources 106 (2002) 284–294.
[5] M. Eikerling, A.A. Kornyshev, Modelling the performance of the cathode catalyst layer of polymer electrolyte fuel cells, J. Electroanal. Chem. 453 (1998) 89–106.

[6] Q. Wang, M. Eikerling, D. Song, Z. Liu, T. Navessin, Z. Xie, S. Holdcroft, Functionally graded cathode catalyst layers for polymer electrolyte fuel cells: I. Theoretical modeling, J. Electrochem. Soc. 151 (2004) A950–A957.

[7] K. BRroka, P. Ekduge, Modelling the PEM fuel cell cathode, J. Appl. Electrochem. 27 (1997) 281–289.

[8] E.M. Ryan, P.P. Mukherjee, Mesoscale modeling in electrochemical devices—a critical perspective, Prog. Energy Combust. Sci. 71 (2019) 118–142.

[9] L. Chen, Y.-L. Feng, C.-X. Song, L. Chen, Y.-L. He, W.-Q. Tao, Multi-scale modeling of proton exchange membrane fuel cell by coupling finite volume method and lattice Boltzmann method, Int. J. Heat Mass Transf. 63 (2013) 268–283.

[10] G. Wang, P.P. Mukherjee, C.-Y. Wang, Direct numerical simulation (DNS) modeling of PEFC electrodes: Part I. Regular microstructure, Electrochim. Acta 51 (2006) 3139–3150.

[11] G. Wang, P.P. Mukherjee, C.-Y. Wang, Direct numerical simulation (DNS) modeling of PEFC electrodes: Part II. Random microstructure, Electrochim. Acta 51 (2006) 3151–3160.

[12] P.P. Mukherjee, C.-Y. Wang, Direct numerical simulation modeling of bilayer cathode catalyst layers in polymer electrolyte fuel cells, J. Electrochem. Soc. 154 (2007) B1121–B1131.

[13] S.H. Kim, H. Pitsch, Reconstruction and effective transport properties of the catalyst layer in PEM fuel cells, J. Electrochem. Soc. 156 (2009) B673–B681.

[14] K.J. Lange, P.-C. Sui, N. Djilali, Pore scale simulation of transport and electrochemical reactions in reconstructed PEMFC catalyst layers, J. Electrochem. Soc. 157 (2010) B1434–B1442.

[15] N.A. Siddique, F. Liu, Process based reconstruction and simulation of a three-dimensional fuel cell catalyst layer, Electrochim. Acta 55 (2010) 5357–5366.

[16] K.J. Lange, P.-C. Sui, N. Djilali, Pore scale modeling of a proton exchange membrane fuel cell catalyst layer: Effects of water vapor and temperature, J. Power Sources 196 (2011) 3195–3203.

[17] W. Wu, F. Jiang, Microstructure reconstruction and characterization of PEMFC electrodes, Int. J. Hydrogen Energy 39 (2014) 15894–15906.

[18] L. Chen, G. Wu, E.F. Holby, P. Zelenay, W.-Q. Tao, Q. Kang, Lattice Boltzmann pore-scale investigation of coupled physical-electrochemical processes in C/Pt and non-precious metal cathode catalyst layers in proton exchange membrane fuel cells, Electrochim. Acta 158 (2015) 175–186.

[19] G. Inoue, M. Kawase, Effect of porous structure of catalyst layer on effective oxygen diffusion coefficient in polymer electrolyte fuel cell, J. Power Sources 327 (2016) 1–10.

[20] L. Chen, Q. Kang, W. Tao, Pore-scale study of reactive transport processes in catalyst layer agglomerates of proton exchange membrane fuel cells, Electrochim. Acta 306 (2019) 454–465.

[21] H. Fathi, A. Raoof, S.H. Mansouri, Insights into the role of wettability in cathode catalyst layer of proton exchange membrane fuel cell; pore scale immiscible flow and transport processes, J. Power Sources 349 (2017) 57–67.

[22] W. Zheng, S.H. Kim, The effects of catalyst layer microstructure and water saturation on the effective diffusivity in PEMFC, J. Electrochem. Soc. 165 (2018) F468–F478.

[23] L. Chen, R. Zhang, T. Min, Q. Kang, W. Tao, Pore-scale study of effects of macroscopic pores and their distributions on reactive transport in hierarchical porous media, Chem. Eng. J. 349 (2018) 428–437.

[24] A.Z. Weber, A. Kusoglu, Unexplained transport resistances for low-loaded fuel-cell catalyst layers, J. Mater. Chem. A 2 (2014) 17207–17211.

[25] T.A. Greszler, D. Caulk, P. Sinha, The impact of platinum loading on oxygen transport resistance, J. Electrochem. Soc. 159 (2012) F831–F840.

[26] D.R. Baker, D.A. Caulk, K.C. Neyerlin, M.W. Murphy, Measurement of oxygen transport resistance in PEM fuel cells by limiting current methods, J. Electrochem. Soc. 156 (2009) B991–B1003.

[27] K. Sakai, K. Sato, T. Mashio, A. Ohma, K. Yamaguchi, K. Shinohara, Analysis of reactant gas transport in catalyst layers; effect of Pt-loadings, ECS Trans. 25 (2009) 1193–1201.

[28] K. Kudo, T. Suzuki, Y. Morimoto, Analysis of oxygen dissolution rate from gas phase into nafion surface and development of an agglomerate model, ECS Trans. 33 (2010) 1495–1502.

[29] J.P. Owejan, J.E. Owejan, W.B. Gu, Impact of platinum loading and catalyst layer structure on PEMFC performance, J. Electrochem. Soc. 160 (2013) F824–F833.

[30] T. Suzuki, K. Kudo, Y. Morimoto, Model for investigation of oxygen transport limitation in a polymer electrolyte fuel cell, J. Power Sources 222 (2013) 379–389.

[31] L. Hao, K. Moriyama, W. Gu, C.-Y. Wang, Modeling and experimental validation of Pt loading and electrode composition effects in PEM fuel cells, J. Electrochem. Soc. 162 (2015) F854–F867.

[32] Y. Ono, A. Ohma, K. Shinohara, K. Fushinobu, Influence of equivalent weight of ionomer on local oxygen transport resistance in cathode catalyst layers, J. Electrochem. Soc. 160 (2013) F779–F787.

[33] L. Chen, R. Zhang, P. He, Q. Kang, Y.-L. He, W.-Q. Tao, Nanoscale simulation of local gas transport in catalyst layers of proton exchange membrane fuel cells, J. Power Sources 400 (2018) 114–125.

[34] M.H. Shojaeefard, G.R. Molaeimanesh, M. Nazemian, M.R. Moqaddari, A review on microstructure reconstruction of PEM fuel cells porous electrodes for pore scale simulation, Int. J. Hydrogen Energy 41 (2016) 20276–20293.

[35] F.C. Cetinbas, R.K. Ahluwalia, N. Kariuki, V. De Andrade, D. Fongalland, L. Smith, J. Sharman, P. Ferreira, S. Rasouli, D.J. Myers, Hybrid approach combining multiple characterization techniques and simulations for microstructural analysis of proton exchange membrane fuel cell electrodes, J. Power Sources 344 (2017) 62–73.

[36] F.C. Cetinbas, R.K. Ahluwalia, N.N. Kariuki, D.J. Myers, Agglomerates in polymer electrolyte fuel cell electrodes: Part I. Structural characterization, J. Electrochem. Soc. 165 (2018) F1051–F1058.

[37] M. Lopez-Haro, L. Guétaz, T. Printemps, A. Morin, S. Escribano, P.H. Jouneau, P. Bayle-Guillemaud, F. Chandezon, G. Gebel, Three-dimensional analysis of Nafion layers in fuel cell electrodes, Nat. Commun. 5 (2014) 5229.

[38] T. Morawietz, M. Handl, C. Oldani, P. Gazdzicki, J. Hunger, F. Wilhelm, J. Blake, K.A. Friedrich, R. Hiesgen, High-resolution analysis of ionomer loss in catalytic layers after operation, J. Electrochem. Soc. 165 (2018) F3139–F3147.

[39] S. Thiele, T. Fürstenhaupt, D. Banham, T. Hutzenlaub, V. Birss, C. Ziegler, R. Zengerle, Multiscale tomography of nanoporous carbon-supported noble metal catalyst layers, J. Power Sources 228 (2013) 185–192.

[40] C.V. Rao, B. Viswanathan, Monodispersed platinum nanoparticle supported carbon electrodes for hydrogen oxidation and oxygen reduction in proton exchange membrane fuel cells, J. Phys. Chem. C 114 (2010) 8661–8667.

[41] R. Zhang, T. Min, L. Chen, Q. Kang, Y.-L. He, W.-Q. Tao, Pore-scale and multiscale study of effects of Pt degradation on reactive transport processes in proton exchange membrane fuel cells, Appl. Energy 253 (2019) 113590.

[42] K. Kudo, Y. Morimoto, Analysis of oxygen transport resistance of nafion thin film on Pt electrode, ECS Trans. 50 (2012) 1487–1494.

[43] T. Mashio, H. Iden, A. Ohma, T. Tokumasu, Modeling of local gas transport in catalyst layers of PEM fuel cells, J. Electroanal. Chem. 790 (2017) 27–39.

[44] R.E. Cunningham, R.J.J. Williams, Diffusion in Gases and Porous Media, Plenum, New York, 1980.

[45] Y.-T. Mu, Z.-L. Gu, P. He, W.-Q. Tao, Lattice Boltzmann method for conjugated heat and mass transfer with general interfacial conditions, Phys. Rev. E 98 (2018) 043309.

[46] S.Y. Chen, G.D. Doolen, Lattice Boltzmann methode for fluid flows, Ann. Rev. Fluid Mech. 30 (1998) 329–364.

[47] J. Zhang, Lattice Boltzmann method for microfluidics: models and applications, Microfluid. Nanofluid. 10 (2011) 1–28.

[48] L. Chen, Q. Kang, Y. Mu, Y.-L. He, W.-Q. Tao, A critical review of the pseudopotential multiphase lattice Boltzmann model: methods and applications, Int. J. Heat Mass Transf. 76 (2014) 210–236.

[49] J.-W. Luo, L. Chen, T. Min, F. Shan, Q. Kang, W. Tao, Macroscopic transport properties of Gyroid structures based on pore-scale studies: permeability, diffusivity and thermal conductivity, Int. J. Heat Mass Transf. 146 (2020) 118837.

[50] L. Li, R. Mei, J.F. Klausner, Lattice Boltzmann models for the convection-diffusion equation: D2Q5 vs D2Q9, Int. J. Heat Mass Transf. 108 (2017) 41–62.

[51] F.C. Cetinbas, S.G. Advani, A.K. Prasad, A modified agglomerate model with discrete catalyst particles for the PEM fuel cell catalyst layer, J. Electrochem. Soc. 160 (2013) F750–F756.

[52] R.M. Darling, A hierarchical model for oxygen transport in agglomerates in the cathode catalyst layer of a polymer-electrolyte fuel cell, J. Electrochem. Soc. 165 (2018) F571–F580.

[53] W. Sun, B.A. Peppley, K. Karan, An improved two-dimensional agglomerate cathode model to study the influence of catalyst layer structural parameters, Electrochim. Acta 50 (2005) 3359–3374.

[54] E. Antolini, L. Giorgi, A. Pozio, E. Passalacqua, Influence of Nafion loading in the catalyst layer of gas-diffusion electrodes for PEFC, J. Power Sources 77 (1999) 136–142.

[55] G. Sasikumar, J.W. Ihm, H. Ryu, Dependence of optimum Nafion content in catalyst layer on platinum loading, J. Power Sources 132 (2004) 11–17.